Defense Technical Information Center Compilation Part Notice

ADP020324

TITLE: Design and Testing of the Minotaur Advanced Grid-Stiffened Fairing

DISTRIBUTION: Approved for public release, distribution unlimited

This paper is part of the following report:

TITLE: Proceedings of the International Conference on Composite Structures [12th] [ICSS/12] Held in Melbourne, Australia on 17-19 November 2003

To order the complete compilation report, use: ADA439334

The component part is provided here to allow users access to individually authored sections of proceedings, annals, symposia, etc. However, the component should be considered within the context of the overall compilation report and not as a stand-alone technical report.

The following component part numbers comprise the compilation report:
ADP020288 thru ADP020363

Design and testing of the Minotaur advanced grid-stiffened fairing

P.E. John Higgins [a,*], Peter Wegner [a], Adrian Viisoreanu [b], Greg Sanford [c]

[a] Air Force Research Laboratory, Space Vehicles Directorate, 3550, Aberdeen Avenue, SE, Kirtland AFB, NM 87117-5776, USA
[b] The Boeing Company, Phantom Works, Seattle, WA, USA
[c] CSA Engineering, 3550, Aberdeen Avenue SE, Kirtland AFB, NM 87117-5776, USA

Available online 1 June 2004

Abstract

A composite grid-stiffened structure concept was selected for the payload fairing of the Minotaur launch vehicle. Compared to sandwich structures, this concept has an advantage of smaller manufacturing costs and lighter weight. To reduce weight the skin pockets are allowed to buckle visibly up to about 0.5 cm peak displacement.

Various failure modes were examined for the composite grid-stiffened structure. The controlling criterion for this design was a joint failure in tension between the ribs and skin of the structure. The identification of this failure mechanism and the assessment of bounding strains required to control it required extensive test and analysis effort. Increasing skin thickness to control skin buckling resulted in reduced strains between the skin and ribs.

Following the identification of the relevant failure criteria, a final design for the fairing was generated. The resulting 6 m tall fairing was constructed of a tow-placed carbon fiber composite grid structure that was over-wrapped to create a laminated skin. Upon completion of curing and machining, the fairing was cut in half to create the classic "clam-shell" fairing. Static qualification testing demonstrated the structural integrity of the fairing, thereby proving the design and manufacturing process. Loads were applied incrementally in a static loading scenario. The applied load envelope exceeded worst-case dynamic flight conditions with an added safety factor of 25%. At peak load the fairing maintained structural integrity while remaining within the required displacement envelope for payload safety.

Data were collected during the test from a variety of sensors including traditional displacement transducers and strain gages. In addition, full field displacement was monitored at critically loaded fairing sections by means of digital photogrammetry. This paper summarizes the test results, presents the overall performance of the fairing under the test loads, correlates test response and analysis, and identifies lessons learned.

Work continues at the Air Force Research Laboratory (AFRL) and Boeing to identify means of further controlling tensile failure of the un-reinforced polymer bonded joint between the ribs and skin. Stiffening of skin adjacent to the joints and introduction of lightweight foam jackets at the interior of the fairing both show promise of delaying joint failure to higher loads.
Published by Elsevier Ltd.

Keywords: Grid-stiffened; Buckling; Failure criteria; Testing; Composite; Fairing

1. Introduction

Over the past 4 years the Air Force Research Laboratory has worked with SMC Det 12 at Kirtland AFB, New Mexico; Boeing Phantom Works in Seattle, Washington; and Orbital Sciences in Phoenix, Arizona, to develop manufacturing procedures, design requirements and a comprehensive design basis to produce a new fairing for the Minotaur launch vehicle. Composite grid-stiffened structures consist of ribs co-cured on a laminated skin as shown in Fig. 1. The skin is allowed to buckle, resulting in localized, non-linear structural behavior (as detailed in Ref. [2]). Both the ribs and the skin are laid using automated tow-placing equipment, yielding lower manufacturing costs compared with a sandwich design. The resulting fairing design is also significantly lighter (on a per volume basis) than an existing smaller sandwich design for the Minotaur launch vehicle fairing. The skin buckling patterns tend to peel the skin from the ribs. Once a rib disbonds, the structural integrity of the structure is compromised. Tests show the joint is the critical component of this

* Corresponding author.
E-mail address: john.higgins@kirtland.af.mil (P.E. John Higgins).
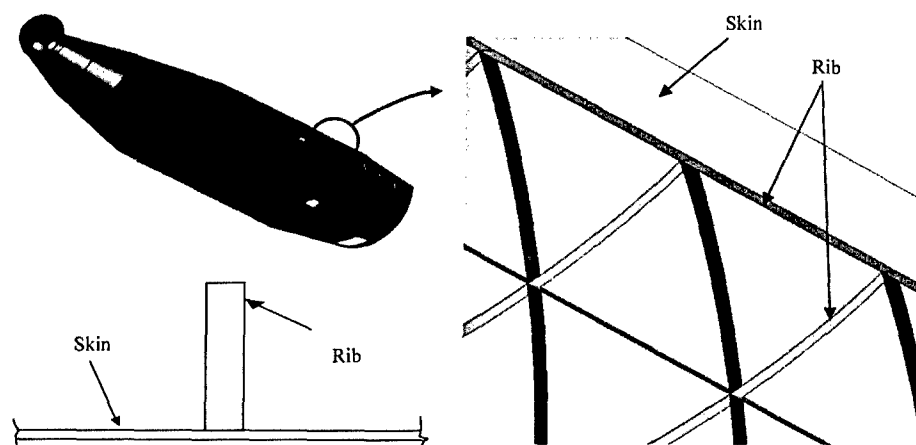
Fig. 1. Minotaur fairing composite grid-stiffened structure.

design. A critical failure criterion was identified for the rib to skin joint, and the design of the Minotaur fairing was primarily driven by the need to control this criterion. During the summer of 2002, the first such composite grid-stiffened fairing design was approved by this team and manufactured in Seattle by Boeing. The fairing was shipped to the AFRL at Kirtland AFB, New Mexico, in early November. Two Flight Qualification tests were performed using a load frame and instrumentation system developed by AFRL. Results of these tests are summarized and recommendations for further system development are discussed. The overall conclusion drawn from this testing is that the fairing design is structurally sound and suitable for further flight development. The first launch demonstration of the new fairing is scheduled for the summer of 2004.

Fig. 2. Joint loads.

2. Failure criteria

Failure criteria checked for this composite grid-stiffened structure include: (1) max strain, (2) global buckling, (3) joint failure resulting from shear, (4) joint failure resulting from skin pull-off (tension), and (5) joint failure resulting from skin peeling or bending (see Ref. [1] for more details). While the first two criteria are common to all composite structures, the last three are specific to the grid-stiffened panels. The loads acting on connecting elements drive the joint failure: F_R the radial pull-off load, F_z the shear load, and M_z the bending moment (Fig. 2).

Shear joint failure. The shear load is transferred to the skin through the adhesive layer. The shear load in the rib element is readily available from the results of the finite element analysis and is used to calculate the interlaminar shear stress.

Pull-off joint failure happens when the tensile strength of the adhesive layer between the rib and skin is exceeded. This failure mode could become critical for very
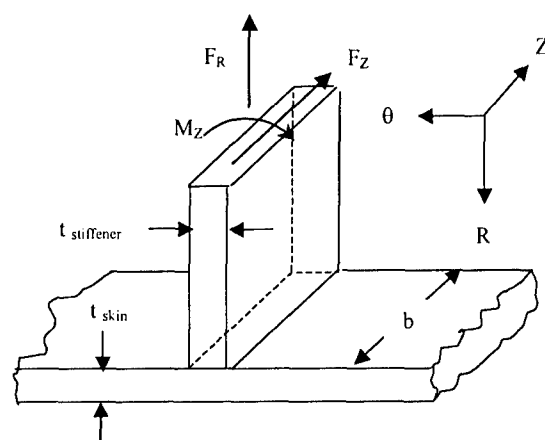
thick skins that have high bending stiffness, but is not critical for aerospace structures.

Peel-off joint failure is the critical criterion for many aerospace structures that use thin skins. The bending moment M_z causes the skin to peel-off from the rib. Skin buckling causes a sharp increase of the bending moment. For thin structures skin peel-off occurs after local skin buckling and usually happens before the other criteria become critical. The failure initiates in the fillet radius that is made only from resin (Fig. 3). T-specimen tests were used to determine the critical strain in the fillet radius. Both the first strain invariant J1 and Von Mises strain could be used for this purpose. Using T-specimens to develop an allowable fillet radius strain offers an advantage by including the effects of manufacturing imperfections and thermal residual strains similar to the actual part. The number of T-specimens was not large enough to determine the allowable strain through statistical analysis. A $J1_{allowable} = 0.7\ J1_{average}$ was selected after calibration with three large panel tests. This $J1_{allowable}$ was used for sizing the Minotaur fairing. The joint loads from the coarse mesh panel model were
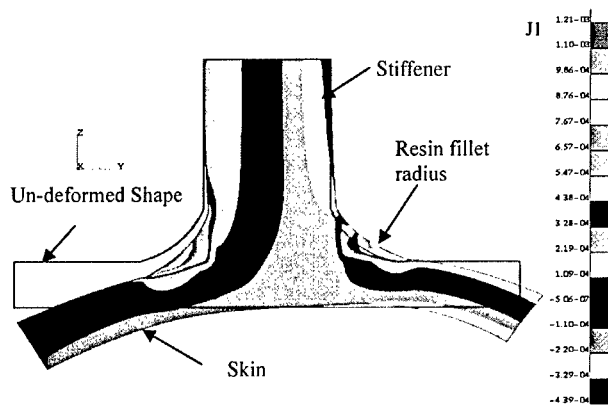
Fig. 3. Joint first strain invariant (J1).

mesh of the detailed model is orders of magnitude finer than the panel mesh and, therefore, has a very different stiffness. Enforcing the displacements of the coarse mesh model on the fine mesh joint model would yield unreliable results.

The loads boundary approach on the other hand is less sensitive to the change in stiffness. The joint loads were obtained as free body grid point forces applied to the elements at each side of the joint. The joint loads for each skin element were reduced at a point located at the distance W from the joint and then applied to the detailed joint model (Fig. 4). Since in our application the rib was much thicker than the skin, it was practical to constrain the displacements of the rib top section rather than applying boundary loads at that section. This also solved the problem of constraining the free body motion of the detailed joint model.

applied to a detailed joint model. The J1 obtained from the detailed joint model is compared with the allowable strain to determine the joint margin of safety. J1$_{average}$ was found by applying the average specimen failure load to a fine mesh model and assessing the peak J1 value for that calculation.

Theoretically the transition between the coarse mesh panel model and fine mesh detail joint model could be done through displacements or loads. However, the

3. T-specimen tests

T-specimens were fabricated and tested to determine the strength of the rib/skin joint. Skin pocket buckling induces a bending load at the rib/skin joint, and the test
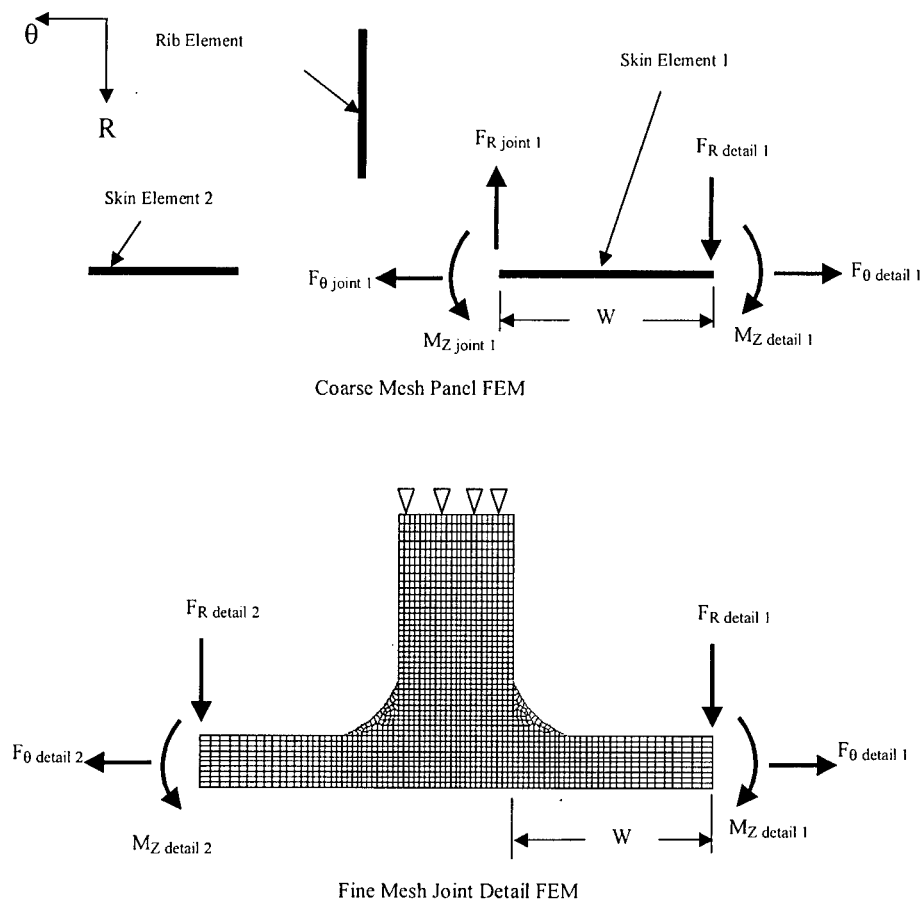

Fig. 4. Application of boundary loads to joint detailed model.

fixtures were designed to induce similar loading at the joint. Specimens with three different skin thicknesses were tested: 3-ply, 6-ply and 8-ply skins.

There was some curvature to the skin because the specimens were cut from the same 60-in. diameter cylindrical structures as the test panels. The specimen rib was clamped between parallel steel plates with serrated faces. There was no indication of slippage between rib and clamp during the tests. A tensile load was applied to the rib, which induced bending in the skin. Large skin deflections occurred, as shown in Fig. 5, until failure. Failure invariably consisted of separation of the rib from the skin. Failure surfaces (also presented in Fig. 5) show a clean break between skin and rib with small resin ridges remaining on the skin where the radii resin accumulated.

As can be seen in Fig. 6 (a micrograph of the rib/skin joint), the bond line between rib and skin is a layer of resin with resin pockets in the radii. These resin pockets are where the maximum skin bending moment occurs and where failure is believed to initiate.

Test results show that specimen strength increases with skin thickness as expected (Fig. 7). The thicker the skin, the less bending deflection and the lower the peel stress in the resin pocket at the radius. A finite element model of each type of specimen and fixture was created to determine critical strains in the resin at failure loads. Initial cracking was found from the first drop in measured load on each specimen.

4. Analysis of test panels

The peel-off joint failure criteria was calibrated with data from three test panels. Cylindrical grid-stiffened panels with 3-, 6-, and 8-ply skins were loaded in compression and tested to failure. Panel finite element models were constructed and analyzed with MSC.NASTRAN non-linear solution. Enforced displacements were applied on one of the transverse edges, while the other transverse edge had all degrees of freedom con-
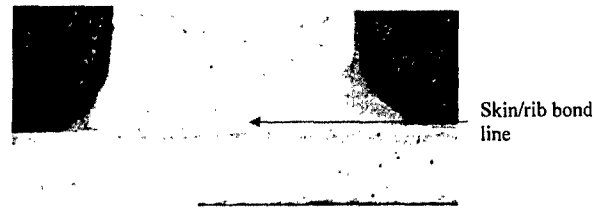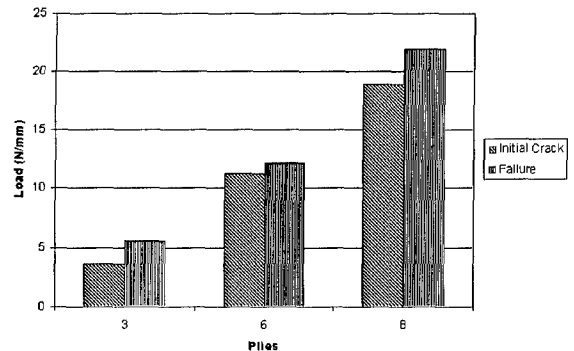

Fig. 6. Photomicrograph of rib/skin joint.

Fig. 7. Strength of T-specimens with 3-, 6-, and 8-ply skin.

strained. Knife-edge support on the longitudinal sides constrains the radial translation (Fig. 8). The load applied to the panel model was increased gradually.

To determine the joint failure, joint loads were extracted at nodes along the ribs and applied to the detailed joint model. The strain invariant J1 in the fillet radius at panel failure was compared with the J1 obtained from the T-specimen tests. This procedure is illustrated in Fig. 9.

The 6-ply skin panel exhibited an early failure of a side axial stiffener that was attributed to a problem with the test fixture. The testing of this panel continued until final failure at a higher load. An allowable J1 of 70% of the T-specimen average J1 would have predicted the joint failure for all three panels, including the initial failure of the 6-ply skin panel (Fig. 10). This J1 allow-
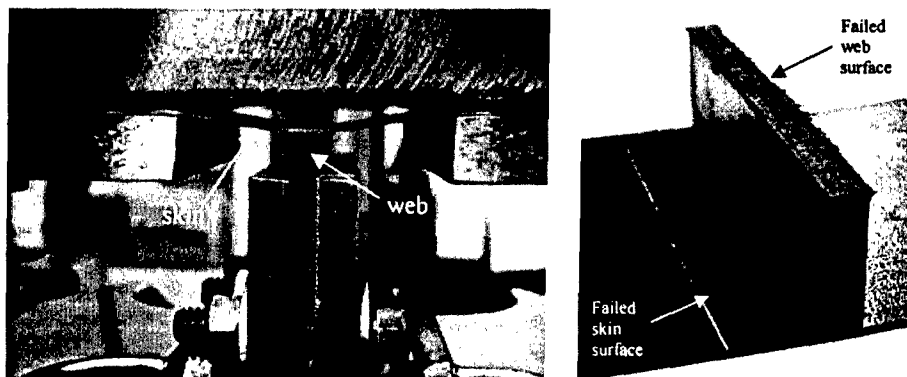

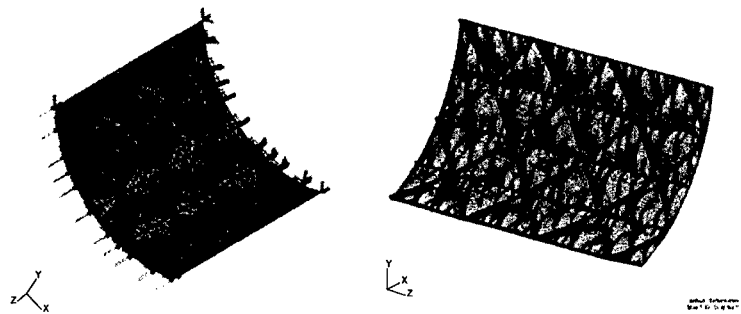Fig. 5. Skin bending during pull test and resulting rib and skin failure surfaces.

Fig. 8. Finite element model and deformed shape of 3-ply skin curved test panel.

Joint Peel-off Criteria:

$J1_{joint} \leq J1_{allowable} \cong 0.7\, J1_{average}$

T specimen Test

$J1_{joint}$

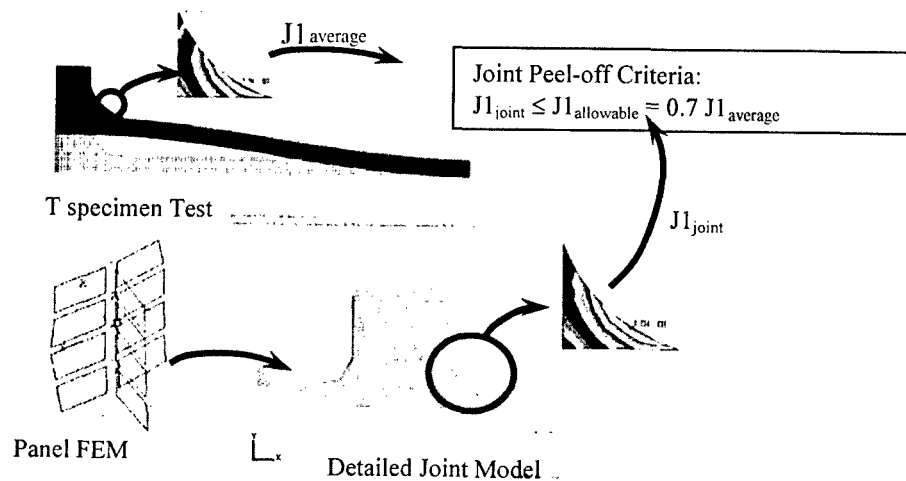Panel FEM

Detailed Joint Model
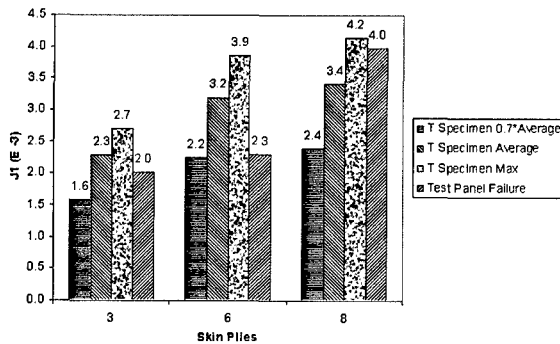
Fig. 9. Joint failure criteria.

Fig. 10. First strain invariant at test panel failure vs. T-specimen tests.

able is conservative, but with the limited test data available it was decided to use it for the sizing of the Minotaur fairing.

5. Analysis of Minotaur fairing

The Minotaur fairing finite element model (Fig. 11) consists of two shells (0–180° and 180–360°) and a nose cap, connected with separation rails. The shell skin is
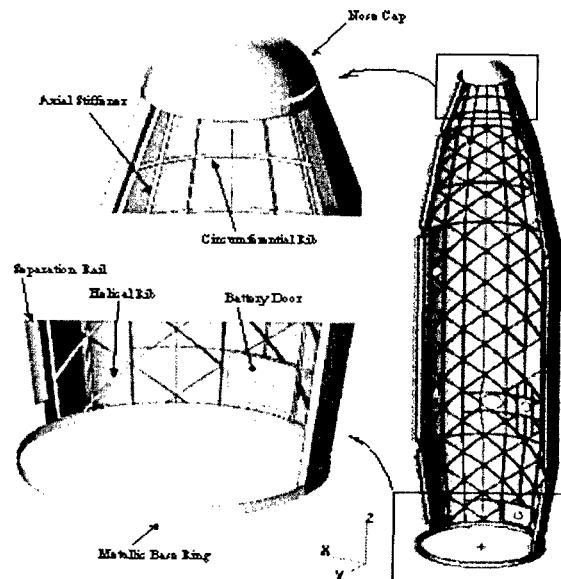

Fig. 11. Minotaur fairing FEM.

reinforced with axial, circumferential and helical stiffeners. Shell elements were used to model the skin, stiffeners, nose cap, and separation rails. Fasteners connect

shells to separation rails, battery door to shell, shells to base ring, shell to nose cap. The fasteners between the nose cap and shell were conservatively modeled with rigid elements. All other fasteners were modeled with a combination of bar, spring, and rigid elements to account for fastener and bearing flexibility. To get a good solution for the skin buckling, the average mesh size is 17 mm, resulting in a model with 116,000 nodes. The mesh size of 6 mm used in the test panel models would have given a more accurate prediction of the skin buckling, but it would not have been practical for the whole fairing.

The first design iterations of the Minotaur fairing were critical to global buckling. As explained in the previous section, when the load approaches global buckling the stiffness matrix becomes singular and the finite element solver fails, which often makes it very difficult to identify where the failure occurs and what part of the structure needs reinforcing. One such example is the forward bi-conic, that is subject to high-pressure loads. Fig. 12 shows the deformed shape of the forward cone at the last converged iteration before global buckling. Adding more circumferential ribs and increasing the skin thickness raised the global buckling load above the ultimate flight load.

The Minotaur fairing was analyzed and sized using the failure criteria described in the previous section. The joint failure due to skin peel-off was the critical failure mode. Joint failure is driven by skin buckling, a highly non-linear phenomena. In one location, increasing the skin thickness from 6 plies to 8 plies resulted in the joint peel-off margin of safety to increase from −0.06 to 1.76. Because of this non-linearity the sizing was often conservative and the strains were low.

Fig. 13 shows the deformed shape of the fairing under qualification test loads. The measured nose displacement was 4.16 cm. The base attachment shifting and rotation contributed 1.02 cm to the total nose displacement. There was also a residual nose displacement of 0.15 cm measured at the end of the test. Correcting for the base shifting and residual displacement, the test nose displacement should have been 4.16−1.02−0.15 = 2.99 cm. This correlates well with the predicted FEM displacement of 2.69 cm.
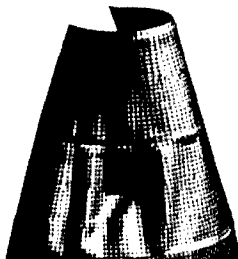

Fig. 12. Global buckling of forward cone.

Fig. 13. Deformed shape under qualification test loads.

6. Fairing qualification test objectives

Design requirements for this fairing and static qualification test loads were developed by the launch contractor for Minotaur missions, Orbital Sciences (OSC). OSC developed a static load criterion requiring four lateral loads and one axial load to be applied proportionally at all times and rising to peak values exceeding calculated flight loads (shear, bending and axial section loads) at all elevations. The lateral loads were to be applied along two separate azimuths in the two test cases. For the first test the lateral loads were applied normal to the plane formed by the separation rails of fairing. The second test applied these loads through the plane of the separation rails. The Qualification Fairing design included numerous standards and representative door panels. One of the larger such doors (a battery access hatch) was located at a point of maximum shear, axial, and bending loads for the first test. The potential for buckling or skin to rib joint failure was considered to be greatest for this test configuration. The second test was oriented such that the aluminum separation rails and thick composite connection pad-ups for these rails were resisting overall bending and represented lower potential risk to the structure (see Ref. [3] for more details).

The major objectives of these two tests were as follows:

A. To observe and confirm that the structure could resist the applied loads without permanent distress or damage.
B. To measure representative strain levels for the applied loads to confirm the nature of the structure response.
C. To measure overall structure displacement under the applied loads to confirm calculated structure stiffness. This measurement is essential to confirm the required flight dynamic displacement envelope is not violated, thereby preventing the fairing and flight payloads from coming into contact.

Secondary objectives of these tests included the following:

A. Provide supplemental instrumentation to insure that intended loads and restraint conditions were met.

B. Assess the nature of unique skin buckling response of the grid-stiffened structure throughout the applied load range at likely regions of distress.

Fig. 15. Typical actuator connections.

7. Test configuration

The Minotaur Fairing Qualification tests were conducted in a general-purpose steel frame load fixture. The test fixture was used previously to flight qualify two separate payload adapter structures; EELV Secondary Payload Adapter (ESPA) for the EELV launch vehicle and a Multiple Payload Adapter (MPA) unit for the Minotaur launch vehicle. To suit the dimensions of the Minotaur fairing, the top cross bracing of the fixture was temporarily removed and an additional 12 feet of vertical column members were inserted at the four vertical uprights of Fig. 14. Actuators connected the load frame to belts that were draped into position with gravity off-load springs. These belts applied the three lower lateral loads to the fairing. These belts distributed load to the fairing through 2 cm thick felt padding on the inside face of the belts. Aluminum spreader bars were provided to prevent contact of belt to fairing on the unloaded face of the fairing. Load angle was confirmed by multiple measurements with a digital inclinometer at 10%, 20%, 30% and 40% of design load. Typical frame to actuator connections and actuator to belt/nose plate connections are illustrated in Fig. 15.

The largest load in each test was applied axially through a strap extending through the interior of the fairing and pulling downward. The nose cone for the fairing was replaced in these tests with a thick aluminum plate (see Fig. 16). The plate rested on a circumferential rib supported by numerous vertical ribs at the nose. This plate was loaded by an internal belt from below and by a fourth (upper) actuator laterally.

The load frame supported the fairing from below on a 3-m diameter, 10 cm thick steel plate resting on steel I-

Fig. 16. Aluminum nose plate test fixture.

beams along 12 azimuths. A cylindrical steel structure containing a man-access port was bolted to the steel plate, and a flexible aluminum ring consistent with the normal fairing attachment system for the Minotaur launch vehicle was bolted between the steel cylinder and the base of the composite fairing (see Fig. 17). The access port in the steel cylinder was used to service the largest actuator loading the internal belt and to port all internal strain gage cables.

Peak static loads were 125% of the design (or flight) load for each load case. In both tests, the upper and middle belts varied by less than 1° from the prescribed values. The angle was adjusted to be at least as great as the prescribed value, and the lateral nose plate actuator loads were increased slightly as needed to insure the correct bending moment at the base of the fairing. Peak axial load was 9070 kg and lateral loads ranged from 1360 to 3175 kg.

8. Active instrumentation, photogrammetry, and photo/video documentation

Each load test provided for 70 channels of strain data located inside the fairing. These strain gages were a mixture of axial strain gage pairs placed at mid-height of helical and axial ribs between intersecting rib nodes and three gage Rosettes placed at central locations between nodes on the skin of the structure. This strain instrumentation was generally located in the lower half of the fairing at locations of maximum overall loading, at points of possible localized strain peaking near door openings, and at points requiring post-manufacturing repairs.
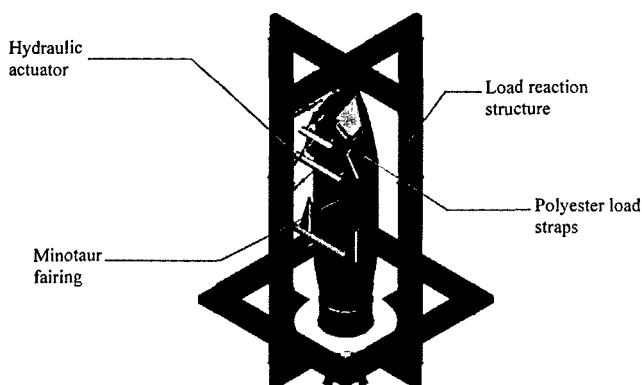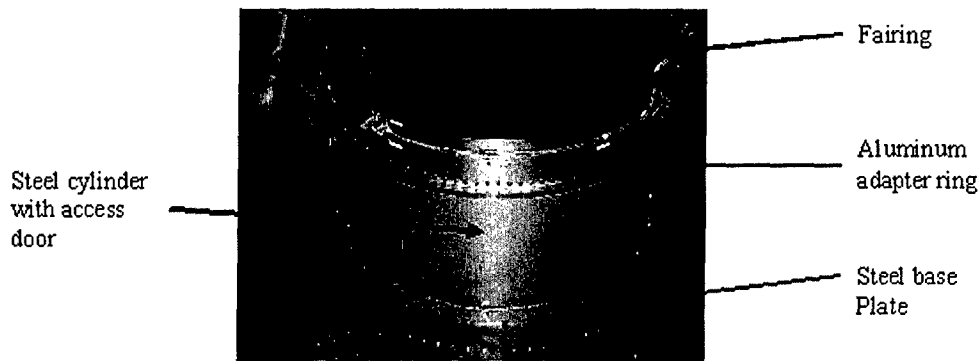

Fig. 14. Test configuration.

Fig. 17. Support structure and aluminum interface.

Each load test provided for 11 LVDT channels to monitor displacements at the base and nose of the fairing. At the base, axial and circumferential motions were measured at 0°, 90°, 180° and 270° azimuths from the direction of lateral load application. At the nose, circumferential displacements were measured at 90° and 270° azimuths from the direction of load application. Additionally one gage at 90° azimuth from the direction of load measured radial nose displacement. The sensors were supported from a Unistrut structure, which in turn was supported from the concrete floor of the laboratory and was unattached to the load frame (see Fig. 18).

A photogrammetry technique as described by NASA [4] was used to measure and confirm the reduction in skin buckling at the critically loaded lower conic section above the battery door in the first load test. A higher tendency for joint delamination was suspected in this region of highest section loading and door induced stress concentration.

Three high-resolution digital cameras were located to capture a field of retro-reflective circular targets illuminated by the integral flash of each Olympus Camedia E-20 camera (see Fig. 19). The target size and camera ranges were adjusted to provide effective sub-pixel target locations using PhotoModeler 4.0 software. The target locations provided by this software were used to assess radial motions of targets located over ribs and on the skin between ribs.
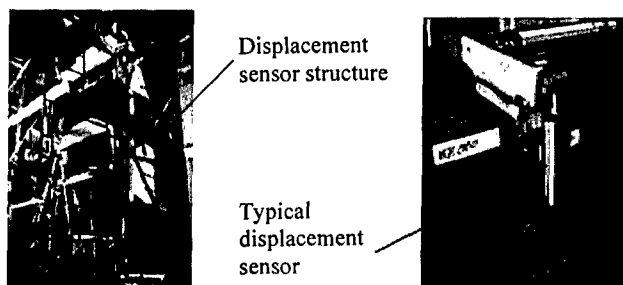

Fig. 18. Unistrut LVDT support structure and typical LVTD Installation.
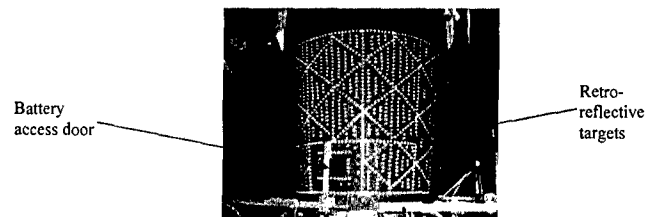

Fig. 19. Retro-reflective targets in Test 1 at base of fairing.

During the course of each test continuous internal video was recorded for the final run up to peak load with close-up documentation of internal rib deformations in regions of large skin deformations during the initial testing to design load. Digital photos also documented these areas of visible skin buckling and other visible areas of concern during testing.

9. Results

In reviewing the strain data for these tests, Fig. 20 is quite typical of the type of linear response observed. These gage pairs were located on the most highly loaded compression ribs near the base of the structure. Very little bending is observed. The peak strain levels in Test 2 are about 40% low despite being positioned lower on the structure than the similar Test 1 gages. This reduced strain probably results from the compression plane alignment of the aluminum separation rail adjacent to this Test 2 gage and the thick composite pad-up at the rail to fairing connection.

Predicted lateral deflections at the nose of the fairing were 27 and 23 mm for Tests 1 and 2, respectively. As seen in Table 1, the actual displacements were about 40–60% greater than anticipated. In the Test 2 orientation, the added bending stiffness provided by the separation rails tended to reduce maximum displacements. Comparing axial LVDT measurements taken at the base of the fairing and noting a relatively large bolted joint slip in the aluminum ring connection at the base of the
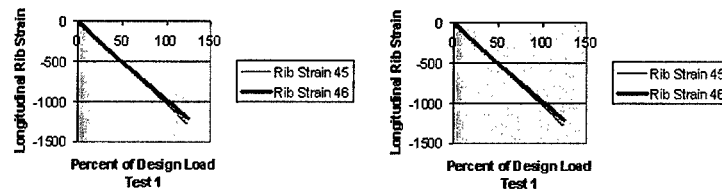
Fig. 20. Compression Rib strain at fairing base—Tests 1 and 2.

Table 1
Fairing lateral displacements (LVDT 1 and 2 along plane of loading and LVDT 3 normal to loading)

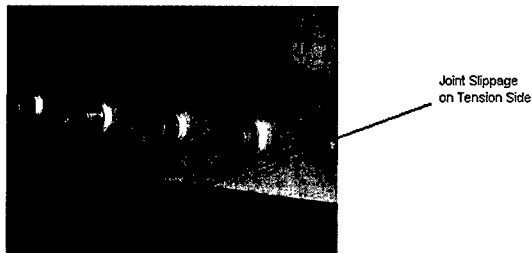|		LVDT 1 (mm)	LVDT 2 (mm)	LVDT 3 (mm)
Load case #1	Initial reading	0.0	0.0	0.0
	125% reading	41.6	41.5	1.0
	Final reading	1.5	1.5	0.0
Load case #2	Initial reading	0.2	0.2	0.0
	125% reading	36.3	36.4	0.0
	Final reading	1.4	1.6	0.0

Fig. 21. Bolted joint slippage at the base of the aluminum ring.

fairing (see Fig. 21), a determination was made that the lateral stiffness of the fairing was well within allowable tolerances. Also, no more than 0.125 mm of lateral nose displacement was seen in either test, suggesting good balance and minimal torque in the applied loads.

The three dimensional models of retro-reflective target locations for Test 1 were compared for the initial (zero) load state and for the peak load state (125% of design). Fig. 22 illustrates the local buckling in the skin at the base of the fairing at the peak load. The radial displacements *do not exceed 0.125 mm* and are localized in the pockets of skin between the ribs. These buckles
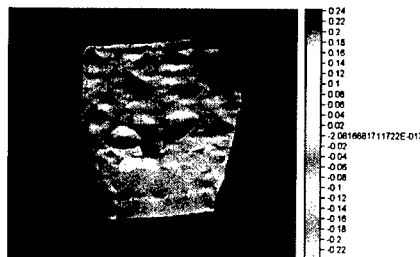

Fig. 22. Radial displacement field at compression side base of the fairing in Test 1.

were not apparent to the eye during the test and do not appear to have influenced the primary response of the structure. Visible buckling was only observed at the middle level of the fairing on the compression side. These results confirm early observations of skin buckling [5] by Boeing.

10. Concepts for the future and lessons learned

An initial philosophy for the design of the Minotaur fairing was to assume that some local or global buckling instability would ultimately control the final design of the structure. Relatively elaborate measures were taken in 2001 to optimize the preliminary design based on a balanced design assumption of inducing simultaneous global, skin, and rib buckling [6]. Initial tests were reasonably consistent with this analysis, but follow-on testing intended to lighten the structure further revealed the deficiency of the joint performance. As currently configured we have high confidence in the structure performance for one-use type applications—launch vehicle adapters and fairings. A logical extension of this technology to aircraft applications or similar lightweight, long-life structures is hampered by the need to insure the integrity of the joint under fatigue cycling, dynamic or impact events, etc. The AFRL and Boeing have evaluated several means of reinforcing or stabilizing the joint response. In general reinforcement is difficult to apply in a manner that significantly improves precrack performance. Joint stabilization has been demonstrated recently to produce some strength gains while improving the nature of the response as well. Fig. 23 illustrates a panel design tested at AFRL this summer. A baseline panel similar to the Minotaur fairing design with a 12 ply lay-up was compared in compression with

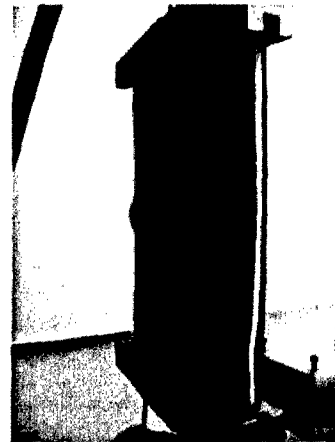Fig. 23. Foam stabilized panel pretest.

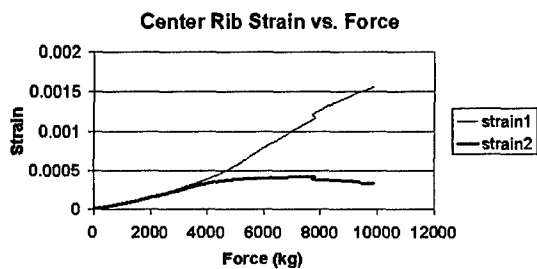Fig. 26. Foam stabilized panel posttest.

Fig. 24. Baseline panel strains.

a panel having the same rib system but an 8 ply lay-up and a stabilizing internal layer of 6 kg/m² Rohacell foam. The foam filled panel has the same mass as the baseline but tested to a 35% higher peak load. Additionally, axial strains measured at either side of the middle of the central ribs indicate a change from rib bending and buckling of that rib in the baseline panel to a stabilized axially loaded behavior in the foam filled modification (Figs. 24 and 25). The baseline design failed by extensive, explosive, joint failure. The foam modified panel failed by a global buckling of the panel followed by delamination of the skin from the ribs at a central hinge (Fig. 26). These types of joint stabilization
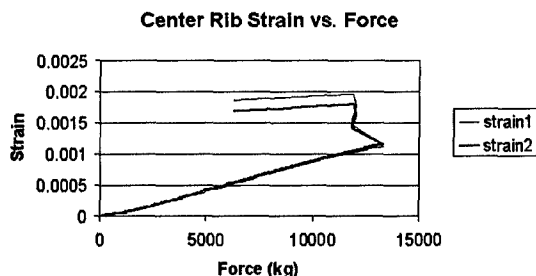

Fig. 25. Foamed panel strains.

features may ultimate lead to greater versatility for this grid-stiffened architecture.

11. Conclusions

The skin peel-off failure mode is specific to thin skin, grid-stiffened composite structures. The failure criteria and allowable strains were developed from small T-specimen tests, calibrated with panel tests and applied to the sizing of the Minotaur fairing. The skin peel-off failure is critical for thin skin panels where the skin is allowed to buckle. Understanding of the failure mechanism of the grid-stiffened composite structures opens the possibility for optimizing the panel geometry and improving the efficiency of the design.

All of the major objectives of these two tests were satisfied. The fairing exhibited no distress of any kind, except for some minor popping noises at lower load level, which were attributed to slippage of bolted joints. Strain response was typically linear and within predicted values for both tests. Overall lateral displacement was within the allowable design criteria and very close to predicted values after giving consideration to unanticipated joint slippage at the base of the fairing.

Indications from displacement gages at the base and nose of the fairing agreed with available load cell data that proper loads were applied and anticipated responses were obtained from the structure. There is no significant indication of asymmetric loading or response.

The peak skin buckling response in this structure did not occur at the base of the fairing as anticipated. The skin thickness varied with elevation in the fairing to maintain a somewhat balanced strain response. The point of greatest radial skin displacement localization was missed; however, the available photogrammetry data clearly demonstrates that skin buckling is present at the higher loads, even though not visibly apparent to

the eye. Neither the low level skin buckling measured at the base of the fairing or the more visible (0.2–0.5 cm) skin buckling observed at mid-heights of the fairing seemed to impact the linear response of the primary load-carrying grid structure.

References

[1] Collier C, Yarrington P, Van West B. Composite, grid-stiffened panel design for post buckling using hypersizer. AIAA 2002-1222.

[2] Wegner PM, Higgins JE, Van West B, Viisoreanu A. Post-buckling test response and analysis of fiber composite grid-stiffened structures. AIAA 2002-1332.

[3] Higgins J, Wegner P, Van West B, Viisoreanu A. Failure criteria for composite isogrid structures. ICCM 14.

[4] Sanford G, Higgins J. Advanced iso-grid fairing qualification test for Minotaur launch vehicle. ICCM 14.

[5] Pappa RS, Jones TW, Black JT, Walford A, Robson S, Shortis MR. Photogrammetry methodology development for Gossamer spacecraft structures. NASA/TM-2002-211739.

[6] Van West BP, Capps CD, Voth MD, Saint Clair JM. Instrumentation and empirical assessment of post-buckling response in grid-stiffened structures. AIAA 2002-1733.